Oceanography Magazine Submission

An overview to modeling, characterizing, and predicting the effects of internal gravity waves on acoustic propagation at basin to global scales

Martha C. Schönau[1*], Luna Hiron[2], John Ragland[3], Keshav J. Raja[2], Joseph Skitka[4], Miguel S. Solano[5], Xiaobiao Xu[2], Brian K. Arbic[4], Maarten C. Buijsman[5], Eric P. Chassignet[2], Emanuel Coelho[1], Robert W. Helber[6], Jay F. Shriver[6], Jason E. Summers[3], Kathryn L. Verlinden[1], Alan J. Wallcraft[2]

[1]Applied Ocean Sciences (AOS), LLC

[2]Center for Ocean-Atmospheric Prediction Studies, Florida State University

[3]Applied Research in Acoustics LLC (ARiA)

[4]Department of Earth and Environmental Sciences, University of Michigan

[5]School of Ocean Science and Engineering, The University of Southern Mississippi

[6]Naval Research Laboratory, Ocean Dynamics and Prediction

[*]Corresponding author: martha.schonau@appliedoceansciences.com.

Abstract:

Underwater acoustic propagation depends on ocean temperature, salinity, pressure, and topography. The realistic representation of the ocean state and its underlying dynamics within ocean models is essential to achieve accurate underwater acoustic propagation modeling and prediction. Stratified, high-resolution global ocean models that include tidal forcing have only been developed in the last two decades. Tidal forcing introduces internal tides and generates higher frequency (supertidal) internal waves. The solutions in such simulations include both higher and lower internal-wave vertical modes, where higher modes have more vertical structure. This project used global, basin-scale, and idealized HYbrid Coordinate Ocean Model (HYCOM) simulations as well as regional Massachusetts Institute of Technology general circulation model (MITgcm) simulations to examine the impacts of tidal inclusion on sea surface height variability, the propagation and dissipation of internal-wave energy, and the sensitivity of internal wave modeling to vertical and horizontal grid spacing. Sound speed, acoustic parameters, and acoustic propagation were compared between tidally-forced simulations and simulations without tidal forcing. Tidal forcing causes variability in acoustic properties at semidiurnal timescales. Deep learning algorithms successfully replicated some of the acoustic variability at test locations

through generation of a “tidal” simulation output from global HYCOM without tidal forcing. The cross-disciplinary effort between ocean modeling and acoustic assessment elucidated the impacts of certain ocean modeling choices (e.g., vertical and horizontal grid spacing, the hydrostatic assumption, and others) on underwater acoustics propagation.

1. Introduction

Sound is a pressure wave, and its speed and path are dictated by the medium through which it travels. Underwater acoustic propagation—the movement of sound below the ocean surface—depends on seawater compressibility and density which are determined by the temperature, salinity, and pressure. There are a variety of processes that impact the thermohaline structure of the upper ocean. These processes include energy input from wind, salinity evolution from evaporation and precipitation, temperature evolution from ocean-atmosphere heat exchange, spatial and temporal variability of large-scale ocean currents, advection of mesoscale ocean eddies, and mixing arising from various processes including breaking internal tides and internal waves (Siedler et al., 2013). Near-inertial internal gravity waves (IGWs) induced by higher frequencies in the wind forcing, and internal tides induced by tidal flow over topographic features, are thought to break and dissipate at vertical scales of order 1 m. IGW variability is not well-captured in many global ocean simulations, which may have incomplete forcing (e.g., a lack of tidal forcing) or may parameterize, rather than resolve, processes that happen at finer scales due to insufficient horizontal and/or vertical discretizations. The goals of the Task Force Ocean (TFO) Office of Naval Research (ONR) funded project to model, characterize, and predict the effects of internal gravity waves on acoustic propagation on basin to global scales, abbreviated “TFO-HYCOM” because of the primary usage of HYbrid Coordinate Ocean Model (HYCOM) simulations, were to improve the modeling of internal tides and waves in global ocean models, characterize the impact of IGWs and internal tides on acoustic propagation, and use machine learning and deep learning (ML/DL) to optimize the predictions of these impacts.

The first part of this integrated research project built on and expanded efforts to improve the modeling of energy transfer and dissipation in the ocean by including tidal motions in global ocean models (Arbic et al., 2012, 2018; Arbic, 2022). Barotropic tidal models in a constant-density ocean have been available since the 1970s, but only in the last two decades has the increase in computational power allowed accurate modeling of tides in a stratified ocean. In a stratified ocean, barotropic tidal flow over topographic features generates vertical motions at the interfaces between different density layers, yielding internal tides, also known as baroclinic tides. Nonlinear interactions between near-inertial motions and internal tides create a continuum spectrum (Garrett and Munk 1979) of higher-frequency (supertidal) IGWs. Low-vertical-mode near-inertial waves, internal tides, and IGW continuum motions propagate throughout the ocean and dissipate when further nonlinear interactions yield short vertical-scale motions that overturn and break. Global internal wave simulations have evolved from uniform two-layer (Arbic et al., 2004) or multilayer stratification (Simmons et al., 2004) in the horizontal direction to the inclusion of realistic horizontally varying stratification by embedding tidal forcing in ocean general circulation simulations. The global distribution of internal tides and IGWs is not uniform (see for example Figure 1), with greater energy near topography and ocean boundaries (Garrett and Kunze, 2007). IGWs can also propagate long distances, impacting the ocean state away from their generation site.

A main goal of the TFO-HYCOM project was to understand the energy transfer between IGW modes, and to evaluate the ability of models at various vertical and horizontal grid spacings to capture this transfer. A primary tool for this project has been global simulations of HYCOM. HYCOM is a primitive equation ocean general circulation model (Bleck, 2002; Chassignet et al., 2003) and HYCOM serves as the dynamical core of the operational global ocean forecast model of the United States Navy (Metzger et al., 2014). In recent years, data assimilation of mesoscale eddies has improved the mesoscale ocean state predictability of HYCOM (Cummings et al., 2013) and the use of techniques from the data-assimilation community has improved the accuracy of barotropic tides (Ngodock et al., 2016). Some of the research for this project also used very-high-resolution simulations of the Massachusetts Institute of Technology general circulation model (MITgcm; Marshall et al., 1997). In one aspect of our research aimed at understanding internal wave energy cascades and dissipation (see latter half of Section 2.2), we used a high-resolution hydrostatic regional simulation of MITgcm with tidal forcing included, and in another aspect, aimed at understanding the impacts of nonhydrostatic assumption on acoustics (see Section 3.2), we used a high-resolution nonhydrostatic simulation.

The TFO-HYCOM team that focused on improving IGW modeling is composed of researchers from the Naval Research Laboratory (NRL), Florida State University (FSU), The University of Southern Mississippi (USM), and University of Michigan (U-M), each with a complementary research focus for the project. The NRL team provided global HYCOM simulations at 1/25º horizontal grid spacing. FSU researchers performed higher horizontal grid spacing (1/50º) North Atlantic basin simulations and idealized simulations with finer horizontal and vertical grid spacing (1 km and up to 128 vertical layers) to study the impact of vertical, horizontal, and bathymetry grid spacing, tidal forcing, and data assimilation on IGWs in HYCOM. USM researchers examined kinetic energy content and transfer between different IGW modes, while U-M researchers further examined the theory of IGW nonlinear energy transfer and dissipation in very-high-resolution regional simulations of MITgcm. In Section 2, we provide a brief description of the HYCOM simulations and summarize the goals and findings of each team to improve IGW modeling.

As advances are made to include tidal forcing in global models, the impact of these processes on underwater acoustic propagation is of interest for a range of applications, such as sonar performance prediction, source localization for bioacoustics, acoustic tomography, and underwater acoustic communications. IGW energy cascades to larger (subtidal) and smaller (supertidal) scales, which leads to mesoscale differences between the simulations at length scales of 100s of kilometers, and temperature and salinity variance at shorter length scales. These in turn impact acoustic propagation. For the TFO-HYCOM project researchers from NRL and Applied Ocean Sciences (AOS) assessed acoustic prediction parameters and acoustic transmission loss using global HYCOM model results with and without tidal forcing. They quantified the impact of the inclusion of tidal forcing on acoustic propagation and discussed these impacts in the context of IGW processes. They compared these results to observations and investigated their sensitivity to horizontal and vertical resolutions.

Finally, TFO-HYCOM project researchers from Applied Research in Acoustics (ARiA) used deep learning (DL) algorithms to derive a tidal ocean state from HYCOM model results without tidal forcing. High-resolution ocean models that include tidal forcing are computationally expensive. DL can be used to parameterize, optimize, and predict the impacts of internal waves on ocean acoustics without high-resolution modeling, and thus may be used in the future to predict the impact of IGWs and tidal forcing on acoustics where ocean modeling may be limited.

2. Improvements to internal wave modeling

HYCOM is the backbone of the operational forecasting system of the U.S. Navy (Chassignet et al., 2009; Metzger et al., 2014). The Navy HYCOM simulations use a hybrid vertical-coordinate system that is isopycnal in the deep ocean and employs depth coordinates (z-coordinates) to resolve the surface mixed layer. The simulations transition to terrain following coordinates in shallow water. The simulations have realistic atmospheric forcing from the Navy Global Environmental Model (NAVGEM) (Hogan et al., 2014) with 60 atmospheric levels over a height of 19 km, 0.17º horizontal grid spacing, and 3-hourly wind forcing. HYCOM simulations analyzed in this paper have been run with or without data assimilation and with or without tidal forcing. To account for numerical errors in the tidal solution caused by imperfect topography and damping terms, an Augmented State Ensemble Kalman Filter (ASEnKF) can be used to perturb the tidal forcing (Ngodock et al., 2016), yielding a globally averaged RMS sea surface height error of 2.6 cm for HYCOM measured against the TPXO satellite-altimetry-constrained barotropic tide model (Egbert et al., 1994).

Several studies have been published on the energetics of IGWs in HYCOM (e.g., Buijsman et al., 2020; Luecke et al., 2020; Raja et al., 2022; Arbic et al., 2022; Arbic 2022). These have focused on solutions without data assimilation. Data-assimilative simulations create spurious waves that overlap at tidal and inertial band frequencies and propagate as low-mode near-inertial waves. Further investigations have revealed that as the model adjusts to the insertion of data-derived increments it generates spurious near-inertial waves (Raja et al., 2023). The interaction of these spurious IGWs with other motions and their eventual dissipation alters the ocean energetics. Hence, for much of the TFO-HYCOM project, we used non-assimilative HYCOM simulations to study the energetics of internal tides (Buijsman et al., 2020) and near-inertial waves (Raja et al., 2022), and investigate their acoustic impacts.

2.1 Internal wave modes

The method of vertical modes is often used to describe the dynamics of IGWs in the ocean (Gill 1982) and it forms an important component of our analysis. To summarize this method, IGWs in the ocean can be approximated as a linear superposition of standing waves in the vertical direction and propagating waves in the horizontal direction. Each wave mode has a characteristic length and phase speed (eigenvalue) and vertical structure (eigenfunction) dependent on the frequency of the IGW and vertical stratification (i.e., vertical density gradient or buoyancy frequency). The method of vertical modes then consists of linearizing the momentum equations and solving the resulting eigenvalue problem based on a time-averaged density profile, yielding the eigenvalues and eigenfunctions.

For the modal analyses presented in this study in sections 2.2 and 2.3.1, we used a 30-day global HYCOM simulation with a 1/25° horizontal resolution and 41 layers that was forced by wind and tides but did not include data assimilation (also referred to as Experiment 19.0). We average the density over the simulation period, compute the buoyancy frequency, and solve the linearized eigenvalue problem. We then project the eigenfunctions on the 3D fields every hour to compute the modal amplitude time series for baroclinic velocity and perturbation pressure. These time series are used to compute the energy and energy fluxes of the IGWs for selected frequency bands.

2.2 The impacts of horizontal and vertical grid spacing on IGWs

The effect of horizontal and vertical grid spacing on the representation of internal tides and internal waves has been documented in recent studies (Nelson et al., 2020; Buijsman et al., 2020; Kelly et al., 2021; Thakur et al., 2022). It has been shown in Buijsman et al (2020) that the horizontal resolution of global HYCOM simulations affects the magnitude of the semidiurnal internal wave energy. Decreasing the horizontal grid size from 8 to 4 km increases the internal wave generation and energy density by about 50%. To a large extent, this increase is attributed to an increase in the number of resolved modes, roughly from the first 2 in the 8-km to the first 4 modes in the 4-km simulations. In this section we expand on this analysis by also considering the impact of the vertical resolution on the resolved modes in a 4-km global HYCOM simulation (Buijsman et al., *in prep*) and in idealized simulations of tidal flow over a Gaussian ridge.

We apply existing and newly developed criteria to determine what diurnal, semidiurnal, and supertidal vertical wave modes could be resolved depending on the horizontal and vertical resolution of a 4-km global HYCOM simulation with 41 layers. For the horizontal resolution we used the criterion that a vertical mode is resolved if there were at least 6-8 cells per wavelength (Steward et al., 2017). A similar criterion was applied for the vertical resolution, this is called the first vertical criterion (CZA). However, this criterion is designed for *z*-coordinate models, whereas HYCOM is isopycnal below the mixed layer. Therefore, we apply an additional criterion called CZB. For CZB a vertical mode was considered unresolved if either two horizontal or two vertical velocity eigenfunction zero crossings occurred in the same layer.

The zonal mean of the number of the resolved modes for seafloor depths >2000 m and averaged over 10° latitude bins is presented in Figure 2. Internal wave modes with lower frequencies have longer wavelengths, and hence, they are better resolved by the horizontal resolution. For the lunisolar diurnal internal tide, K_1, eight modes are resolved on average at the equator and the number increases towards 20 modes near the K_1 turning latitude due to the increase in wavelength. The shorter wavelength principal lunar semidiurnal internal tide, M_2, has fewer modes resolved, with a minimum number of about 4 modes resolved at the equator. Of the supertidal frequencies, a shallow water harmonic, M_4 has the most energy. On average, only up to two M_4 modes are resolved.

In contrast to the horizontal resolution, the number of resolved modes is more sensitive to the vertical resolution criteria. If CZA is applied to the hybrid vertical coordinates, mode 1 is barely resolved at the low latitudes and not at all at higher latitudes (Figure 2). In contrast, CZB allows for the resolution of more modes with a maximum of 12 modes resolved at the equator.

Next, we compare these “predictions” (Figure 2**)** to the simulated variance and energetics of the 4-km HYCOM simulation (Buijsman et al., 2023, *in prep*). The horizontal resolution criterion for tidal and supertidal internal waves is quite accurate. For instance, the first two supertidal (M_4) modes capture most of the variance in the 4-km simulation as predicted. CZA is not a good predictor of the number of resolved modes in an isopycnal coordinate model because the HYCOM simulation has variance at many more vertical modes. Although the accuracy of CZB is harder to determine, it predicts the correct trends. For example, the horizontal resolution limits the semidiurnal variance to about four resolved modes at low latitudes, whereas the vertical resolution limits the variance at higher latitudes. This agrees with a recent study by Geoffroy et al. (2022), in which the M2 internal tide variance in a 4-km HYCOM simulation is compared to the variance observed with Argo floats. They find that in the southern oceans HYCOM under-resolves the internal tide modes, which can be attributed to the thicker deep isopycnal layers.

To further investigate the impact of vertical resolution on IGWs in HYCOM, Hiron et al. (2023; *in prep*) performed a set of HYCOM simulations with an idealized configuration, fine horizontal grid spacing (1 km), forced only by the M_2 tidal frequency, and varying vertical grid spacing from 8 to 128 vertical isopycnal layers. The vertical discretization was done by finding the zero-crossings of the u-eigenfunctions for different vertical modes. For example, the interface depths of the 32-layer simulation are the zero-crossings of the u-eigenfunction of the 32nd vertical mode. The simulations were initialized with a density profile from climatology averaged over the Cape Verde area to be representative of the density of the tropics. To generate internal tides, a steep ridge with a Gaussian shape was added in the center of the domain. The criticality of the slope, which is a measure of the ridge steepness normalized by the ray slope of the internal waves, is larger than one, allowing for the generation of nonlinear waves and wave beams (Garrett and Kunze, 2007; Buijsman et al., 2010). Figure 3a shows a snapshot of the vertical velocity for the 128-layer simulation highlighting the region near the ridge where the wave beams are strongest. Figure 3b shows the depth-integrated, vertical kinetic energy (½ $\int w^2 dz$), where w is the vertical velocity, for different vertical discretizations (8-, 16-, 32-, 48-, 64-, 96-, and 128-layer) and averaged over one week. The 8- and 16-layer simulations differ from the others in amplitude and phase. The 32-layer simulation has a similar magnitude as the finer grid-spaced simulations but a different phase. From the 48- to the 128-layer simulations, magnitude and phase are similar across simulations. Strong vertical velocities lead to greater vertical displacement of the isopycnals which can then affect sound speed and, potentially, the acoustic propagation (See Section 3.2). When integrated over the whole domain (0 to 2000 km from the ridge), the tidal barotropic-to-baroclinic energy conversion, the vertical kinetic energy, and the turbulent dissipation were all greatest in the 128-layer simulation and decrease with coarser vertical grid spacing. The results start to converge for the simulations with more than 48 layers, however, this may differ with a change in horizontal grid spacing.

2.3 Energetics of Internal Gravity Waves (IGWs)

2.3.1 Nonlinear internal tides

In the open ocean, low-mode internal tides may decay via wave-wave interactions cascading energy to higher frequencies and wavenumbers (Lamb 2004; Eden et al., 2020). One type of wave-wave interaction that affects the low-mode semidiurnal internal tides, Parametric *Subharmonic* Instability (PSI), has been extensively evaluated in global ocean model simulations (e.g., Ansong et al. 2018). In contrast, the decay of the low-mode internal tide due to *superharmonic* wave-wave interactions (also referred to as nonlinear steepening) has not been thoroughly studied in global simulations. Here we discuss results from Solano et al. (2023, submitted), in which we evaluate the tidal and supertidal energetics, the energy transfers between the tidal and supertidal bands, and interactions between low-mode waves.

The kinetic energy band-passed at semidiurnal and supertidal frequencies are shown in Figure 1a and 1b respectively, and Figure 1c shows the percent of supertidal energy compared to total (tidal+supertidal) energy. The energy at the primary frequencies dominates most of the internal tide spectrum, except along the path of large amplitude internal tides near the equator.

Supertidal KE is more important at lower latitudes (±25°), as seen by the relatively higher energy in the Tropics (Figure 1b), where it accounts for about 5% of the total (tidal+supertidal) energy based on globally averaged values. However, locally in regions such as the Bay of Bengal, the Amazon Shelf, and the Mascarene Ridge, 25-50% of the IGW kinetic energy is found at supertidal frequencies.

We estimate the nonlinear energy transfer from (sub)tidal to supertidal frequencies based on the time-mean and depth-integrated coarse-grained kinetic energy. The nonlinear IGW energy transfer from primary to supertidal frequencies reveals a banding pattern (Figure 4a-c) that agrees well with the horizontal divergence of the supertidal energy flux (Figure 4d-f). In the 3 regions where supertidal energy is high, a regularly spaced banding pattern emerges where energy is transferred from primary to higher-harmonic frequencies at a rate of about 10-50 mW m^{-2} locally. Globally and at low latitudes, internal tides transfer energy to higher harmonics at a rate of about 45 GW, compared to the 500 GW of energy available from barotropic tides (i.e., barotropic to baroclinic conversion).

The banding pattern in Figure 4 suggests a common mechanism for the nonlinear energy scale transfer, which is further investigated by considering the decomposition of vertical modes. The decomposed kinetic energy in Figures 4g-i shows a similar banding pattern that appears only for the superposition of the lowest modes (1+2) but is not seen in the individual modes. This surface intensified pattern suggests that these regions of enhanced transfer to higher-harmonics can be explained by the interactions between mode-1 and mode-2 internal tides, which interfere constructively at the locations of the patches (e.g., their velocities are in phase, increasing the tidal amplitude and steepening the internal tide). The location of these patches is modulated by the slowly varying subtidal current, which affects the vertical stratification and therefore the characteristic speeds of the modes. The amplitudes of these patches are also modulated in time by the spring-neap cycle; the higher amplitude spring tides result in larger energy transfers to higher-harmonics.

2.3.2 Spatial variability in spectral slopes

Sea-surface height (SSH) variability is a useful proxy for mesoscale ocean variability. Comparisons of satellite altimetry to ocean simulation results can be used to quantify the realism of the ocean simulations as well as their sensitivity to the horizontal resolution, and vertical resolutions, and physical parameterizations employed in the simulations. The mesoscale sea surface height (SSH) wavenumber spectral slopes computed from satellite observations exhibit large spatial variability (e.g., Figure 5a, Xu and Fu, 2012; Zhou et al., 2015; Dufau et al., 2016), whereas previously published high-resolution model results lack a comparable spatial variability (e.g., Figure 5e-f; Chassignet and Xu, 2017). The spectral slope represents the relative strength of oceanic flows as a function of length -scales. Motivated by this apparent discrepancy, Xu et al. (2022) investigated the impacts of internal tides, high-resolution bathymetry, and high-frequency atmospheric forcing on the SSH wavenumber spectra in the Atlantic Ocean using a series of 1/50° North and equatorial Atlantic simulations with a realistic representation of mesoscale-to-submesoscale variability and barotropic/baroclinic tides. Their results highlight that the inclusion of internal tides increases high-frequency SSH variability with clear peaks near the tidal characteristic wavelength for the first and second vertical modes, and flattens the spectral slope in the mesoscale range, improving the agreement with observations (Figures 5a-d). The surface signature of internal tides is the most significant in the equatorial Atlantic where there are strong barotropic tides and a strong stratification in the upper layer of the water column and is also seen in the subtropical regions of the eastern North Atlantic. The internal tides are the primary cause of the observed large spatial variability of the spectral slope in the Atlantic. High-resolution bathymetry and high-frequency wind variability have a comparably minor impact on the modeled large-scale SSH variability and SSH wavenumber spectra. On a local scale, however, high-resolution bathymetry details, especially the slope near the shelf break, play an important role in the generation of internal tides.

2.3.3 Spectral fluxes

The IGW spectrum not only involves the transfer of energy between internal wave modes; it also mediates the transfer of oceanic kinetic energy from its injection at large scales in eddies, near-inertial-waves, and tides to the smallest resolved scales. As such, properties of the IGW spectrum depend on the ocean state, including the slowly varying background circulation and surface forcing that may affect vertical stratification. An empirically determined form of the global IGW spectrum has been determined by Garrett and Munk (1979) (the GM spectrum hereafter) but has free parameters to account for regional and seasonal variation. Ongoing research focuses on what determines these parameters and any deviation from the GM form; nonlinear interactions involving IGWs are thought to be of particular importance.

Previous theoretical and idealized work on IGW-IGW interactions has identified some important processes that move energy downscale within the supertidal IGW spectral continuum

(McComas and Bretherton, 1977; Dematteis et al., 2022). These studies did not attempt to analyze eddy-IGW interactions in the same manner as IGW-IGW interactions and imagine the GM spectrum as being shaped primarily by the latter processes. One mechanism, “induced diffusion,” is thought to be particularly important and involves near-inertial and tidal IGWs inducing downscale KE transfer in the supertidal continuum. Skitka et al. (2023, *in review*) used a unique framework of asymmetric spectral kinetic-energy fluxes to diagnose these IGW-IGW interactions along with analogous eddy-IGW interactions from a regional MITgcm ocean simulation in the North Pacific (Nelson et al., 2020; Pan et al., 2020, Thakur et al., 2022).

Among other things, Skitka et al. (2023, *in review*) showed that IGW-eddy interactions induce downscale KE flux within the supertidal IGW continuum in a manner analogous to induced diffusion. This “eddy-induced diffusion” is the dominant mechanism of energy exchange within the IGW supertidal continuum at 2-km horizontal grid spacing that are typical for high-resolution global models, while it is comparable to canonical wave-induced diffusion at the higher 250-m horizontal grid spacing that are achievable in regional models (Figure 6). Finer grid spacing in the vertical and horizontal directions therefore make a large difference in the details of the IGW cascade, including the rate of spectral flux, the dominant mechanisms that contribute to the spectral flux, and the mechanisms and patterns of dissipation. All of these have implications for global models. Further research is needed to fully resolve these mechanisms and understand the sensitivity of oceanic parameters that are relevant to resolving them. For instance, the relative magnitude of eddy-induced diffusion in Figure 6 suggests eddy fields are important (particularly in resolution-limited models) in shaping the IGW spectrum and, in turn, any wave-induced dissipation or mixing that may affect environmental acoustic parameters. Eddy-induced diffusion also may be a key factor in both developing closures for partially resolved IGW continua in global models such as HYCOM, as well as explaining substantial regional variation that has been observed in the IGW spectrum (Polzin and Lvov, 2011).

3. The impact of tidal forcing on acoustic propagation

As light bends in different media, sound refracts whenever environmental factors induce a change in sound speed. Sound speed is impacted by changes in pressure and gradients in temperature and salinity structure that impact density, such as fronts, eddies, currents, vertical stratification, and mixing. Internal tides and gravity waves undulate the water column and mix the column when they break. A tidally-forced ocean model thus will have a sound-speed structure that may be very different from that of a non-tidally-forced ocean model. The question is how acoustic propagation will differ between these two models, and how important the model's horizontal and vertical grid spacing are in capturing these processes?

3.1 Acoustic parameters and propagation in Global HYCOM

The Naval Research Laboratory made available the output from four simulations of the Global HYCOM model, with and without tidal forcing and with and without data assimilation (DA): tidal forcing and no DA (Exp. 19.0), no tidal forcing and no DA (Exp. 19.2), tidal forcing and DA (Exp. 21.6), no tidal forcing and no DA (Exp. 19.1). Global HYCOM was run on 41-density layers at roughly 2-km resolution in latitude and 2-km to 4-km resolution by longitude. Temperature and salinity were interpolated to 101-depth layers to then compute the sound-speed profiles. Hourly output was available for one month from May to June 2019. The four simulations were compared to Spray glider observations in the California Current in the North Pacific (Figure 7). The mean and standard deviation of the sound speed were computed from each simulation at 3-hourly intervals over the region which the glider was profiling. (The glider profiles from the surface to 500 m depth roughly every three hours.) Although this is not a region of large tidal energy, the tidal forcing increased the sound speed variability. The simulation with both tidal forcing and data assimilation compared most closely to observations. However, even without data assimilation, the HYCOM simulation with tidal inclusion performed better than the simulation without tidal forcing.

The sound speed variability at a given depth can be a sign of the sound speed surfaces moving vertically. Global HYCOM can be used to visualize these waves propagating over great distances by following depth changes of the single sound speed surface with time to using a density surface. Figure 7c compares the depth of the 1510 m s^{-1} sound speed surface along a 5000 km transect in the North Pacific across the Luzon Strait, a location of strong internal tide generation owing to a steep topographic ridge (e.g., Alford et al., 2015). At the ridge, located at 1000 km along the transect, internal tides propagate in both directions as seen by the radiating lines in Exp. 19.0 which includes tidal forcing. Sharp topography in the North Pacific causes additional internal tide propagation and interference (e.g., at 4800 km). These undulations are absent in Exp 19.2 which did not include tidal forcing. We do not show the cases that include data assimilation. Although the data-assimilative simulations were closer to observations (Figure

7a), spurious jumps can occur in sound-speed structure during an assimilation window, as discussed in Section 2.

To further examine the impacts of tidal forcing, we compared acoustic transmission loss and acoustic parameters between Global HYCOM simulations in the Amazon Basin. Acoustic parameters are a set of tools that are used to examine the potential impact of physical ocean characteristics on acoustic propagation (Naval Meteorology and Oceanography Command, 1986), a bellwether of the types of propagation that might occur given only the oceanography. When examining the properties of potential surface duct propagation, two acoustic parameters of interest are the sonic layer depth (SLD) and below-layer gradient (BLG). The SLD is defined as the depth of the subsurface sound-speed maximum (e.g., Helber et al., 2008). Above this depth, if the acoustic source is within the layer and the frequency is supported by the layer, sound can potentially be trapped between the surface and the SLD. The BLG, defined as the gradient in sound speed below the SLD, can influence the potential of the layer to retain trapped energy.

In addition to acoustic parameters, running an acoustic propagation model provides direct information on how sound at a given frequency and depth may propagate. Propagation behaviors can be quantified in terms of both transmission loss and acoustic arrival times. For the acoustic model, we used a 1500 Hz, mid-frequency source and a three-dimensional ray-tracing model, Bellhop 3D, available from the Ocean Acoustics Laboratory (Porter, 2011). The acoustic TL provides a relative estimate of acoustic pressure and an estimate of whether the source may be detectable at a certain range.

In the Amazon shelf region, there is propagation of low to high mode internal waves and evidence of a strong semidiurnal tide. The semidiurnal tide causes internal tides to propagate in a northeast direction away from the coast; this can be seen along the line in Figure 4b where energy is transferred to higher harmonics. A virtual acoustic source was placed into the simulations at 20 m depth at 4.1ºN and 44.8ºW, and acoustic TL and acoustic parameters from the sound speed profile were examined along the 60º radial (Figure 8a) in the direction of tidal propagation (Figure 4b). The semidiurnal internal tide creates fluctuations in the SLD and BLG that are absent in the case without tidal forcing, where the depth of the layer is persistently deeper. The SLD is shallower, and the BLG is more gradual in the tidal case, and each shows semidiurnal variability. In the nontidal case there is a deeper SLD.

The ocean sound-speed structure differences between the two models which are hinted at by the SLD and BLG impact the TL in the surface layer. In the tidal case, there is greater TL

(Figure 8a) likely owing to a shallower SLD, particularly from 20 to 23 May. Near the sources, there is sensitivity to this depth, with transmission occurring on a semidiurnal timescale with the SLD undulation. Additionally, the tidal case exhibits higher loss due to sound speed profiles with more structure, that is, gradient changes in the sound speed due to the tidal variations can create less convergent energy. In the nontidal case, there are no periodic fluctuations in TL, only irregular fluctuations associated with submesoscale to mesoscale variability.

The mesoscale differences between simulations with and without tidal forcing make a direct comparison between them problematic. Some of this variability is owing to how the tides interact with the mesoscale field and atmospheric forcing. Correlation coefficients between wind and mixed layer depths in the Amazon region were similar between the tides and no-tides simulations, but with differences near the coast where currents and tidal variability were strong. This will be an avenue of future research. The SLD was shallower and semidiurnal fluctuations were present in the tidal case. Snapshots along the 60º radial provide insight into how the differences in sound speed impacted acoustic TL (Figure 8b). The internal tides undulate the pycnocline, causing changes to the vertical sound speed gradient. The effect of the SLD on the TL is relatively straight forward, with greater TL if the source is not in the duct as the duct shoals; but it is less clear how TL is impacted by changes in the BLG (Figure 7c) and by horizontal gradients of sound speed that tidal forcing introduces. The structure of the sound speed profiles (horizontally and vertically) guide the paths of the sound, a smooth profile will result in a greater concentration of energy (less loss) and a profile with many small gradient variations will result in more refracted energy (more loss) throughout the entirety of the waveguide.

3.2 Acoustic impacts of horizontal and vertical grid spacing

Horizontal and vertical grid spacing play a significant role in the ability of models to capture energy transfer in the ocean, and the grid spacing will impact acoustic propagation as well. The acoustic impacts of model horizontal grid spacing were examined along the Mascarene Ridge, where two tidally forced models are compared; the impacts of vertical grid spacing on sound speed was explored using the idealized model described in Section 2.2.

The Mascarene Ridge is a location of nonlinear wave interactions, where solitons are generated and propagate away from the Ridge (Figure 4c, f, i). We employ two-dimensional nonhydrostatic simulations of the MITgcm, with a horizontal grid spacing of 100 m. By comparison, the global HYCOM model (Exp. 19.0; with tides and no DA), is hydrostatic and has a horizontal grid spacing forty-times smaller than that of the MITgcm. Although a direct comparison of the sound-speed structure was not possible, as the HYCOM simulations were initialized with an offset in temperature, the relative difference in acoustic parameters is insightful (Figure 9). Looking at the SLD and BLG, the HYCOM model has a clear semidiurnal signal which fluctuates the SLD up and down twice a day (Figure 9a). The MITgcm simulation has a periodic signal as well, but it is disorganized, with propagation pathways appearing to overlap (Figure 9b). The higher grid spacing of the MITgcm simulation allows nonlinear interactions to occur, and these impact the sound speed structure.

The vertical grid spacing of simulations can also impact internal-wave energy transfer and propagation when tidal forcing is included. To isolate this impact on acoustics, without the confounding challenges of differences in mesoscale eddy fields or initialization states, we used an idealized model (described in Section 2.2). The idealized model was initialized with the same temperature profile, taken from the tropical Atlantic with constant salinity structure. For the sound speed comparison, we used the simulations run on 8-, 16-, 32-, 48-, and 96-isopycnal layers, and then interpolated to constant-depth coordinates. Taking the mean and standard deviation of sound speed over 72-hour timesteps, there are clear differences between the simulations (Figure 9c). The lower vertical grid simulations have a noticeably different mean sound speed and deeper SLD. At lower resolution, the sound speed variability does not resolve the variability near the surface around the thermocline depth or near 1200 m where a deep sound channel can form. These can both impact the strength and distance of acoustic propagation. As the number of layers increases, the sound-speed profiles and their variability converge with very little difference between the 48- and 96-layer simulations. Future investigations into the impacts of horizontal and vertical model grid spacing on acoustics will take place in using realistic regional models.

4. Developing awareness and creating solutions using Deep Learning (DL)

Tidally forced, global ocean models are computationally expensive. In the following section, DL is used to investigate the statistical differences between HYCOM simulations with and without tidal forcing. The goal is to see if one can be generated from the other without numerically solving the physical forcing equations, thus reducing the computational cost. In theory this would allow someone to use an ocean simulation without tidal forcing to generate an ocean state similar to that of a tidal forced ocean simulation, allowing them to better predict acoustic propagation. To do this, we explore if DL can be used to translate the global HYCOM without tides simulation (Exp. 19.0) to a global HYCOM simulation with tides (Exp. 19.2). A Generative Adversarial Network (GAN) (Goodfellow et al. 2014; Creswell et al. 2018) is proposed as a potential solution to this problem.

One of the challenges in this approach is that the ocean has chaotic, turbulent flow; very small perturbations in the environment can lead to large differences in mesoscale eddy structure. These large mesoscale differences between nontidal and tidal model results make it difficult to make direct comparisons between the simulations. This effect is particularly evident in areas in the ocean with large turbulence, such as the Gulf Stream. To address this issue, we consider the HYCOM simulations with and without tidal forcing to be unpaired. This means that we do not compare a specific point in space and time between the two simulations. Instead, we investigate the differences in the statistical distributions of the two simulations for a large region of the globe and see if it is possible to translate from one distribution to another.

4.1 Statistical separation between non-tidal and tidal data

Before developing a DL algorithm that can translate between nontidal and tidal results, the spatial and time dimensions that cause the greatest statistical separation are investigated. To investigate which dimensions have the greatest statistical separation, model results with and without tidal forcing were combined into a single dataset and decomposed into empirical orthogonal functions (EOFs).

For different pairs of dimensions, the orthogonal components of nontidal and tidal model output were computed for HYCOM output between a set range of latitudes and longitudes. The distributions of the coefficients were then visually investigated to search for any separation between nontidal and tidal results. It was found that horizontal slices in latitude and longitude have identical distributions of coefficients for the orthogonal components. This means that for a horizontal slice of the ocean there is no difference between HYCOM simulations with and without tidal forcing.

However, the coefficients for the EOFs that were computed for the time and depth dimensions show notable statistical separation. Figure 10 shows several selected orthogonal components for depth and time for a region off the Amazon shelf. The first three columns of Figure 10 are selected components that do not have statistical separation. These components are responsible for constructing the general structure of water temperature as a function of depth and time that both tidal and nontidal results exhibit. The last three columns represent components that have large differences in the coefficient distributions between the two simulations. Since the coefficients for these components are generally larger for tidal model results, they provide insight into the structures of water temperature as a function of depth and time that characterize tidally-forced model results in this region. This increased coefficient is another statistical way to quantify the increase in upper-ocean variability that occurs when tidal forcing is included in the ocean model, similar to the increase in sound-speed variance that was observed when looking at ocean-acoustic properties.

4.2 Using DL to translate from a non-tidal ocean to a tidal ocean state

General Adversarial Networks (GANs) are a DL technique that tries to learn a transformation from one statistical distribution to another, instead of trying to directly learn a specific distribution. Additionally, the DL model that performs that transformation is trained alongside an adversarial discriminator that is trying to differentiate between actual data and generated data (Goodfellow et al. 2014, Goodfellow et al. 2016). Given the way that GANs are formulated, they are well suited for the problem of translating nontidal results (NT) to tidal (T) results for vice versa.

Since we are considering the HYCOM results with and without tidal forcing to be unpaired data, we need a way to train the networks in a way that does direct comparison between simulations for a specific region with and without tidal forcing. This can be done with cycle-consistency loss. For this method, we train two separate generators and discriminators. One generator, $G_{NT\rightarrow T}(\cdot)$, translates from the non-tidal to the tidal domain, and the other generator, $G_{T\rightarrow NT}(\cdot)$, translates from the tidal to non-tidal domain. The two discriminators try to separate real tidal results from nontidal results that have been translated tidal domain and vice versa. For training, data is translated to the opposite domain, and then translated back to the original domain, $x\hat{}_{NT} = G_{T\rightarrow NT}\ G_{NT\rightarrow T}(\cdot)(x_{NT})$. The cycle-consistency loss is then defined as the L1 distance between the original data sample and the double translated data as shown in the below equation (Zhu et al., 2017):

$$\mathcal{L}_{cycle} = \|x\hat{_{NT}} - x_{NT}\|_1 + \|x\hat{_T} - x_T\|_1$$

The cycle-consistency loss is used in combination with the traditional GAN losses to train the networks. Land values are set to exactly zero, passed through the generator and then turned back into land values. The loss function thus ignores the land values since they have a loss of zero. This technique is like that of Mejjati (2018) but without having to learn an attention mask as the region is known a priori.

4.3 Training the GAN model and results

HYCOM output in the Atlantic Ocean was split into 90% training data and 10% validation data. Validation was chosen in contiguous rectangles with a width of 32 grid spacing in each latitude and longitude. This was done to minimize the degree to which validation samples have multiple adjacent training samples, which would contribute to data leakage and overfitting. Figure 11 shows the original HYCOM model results (i.e., Exp 19.0 and Exp. 19.2) and GAN outputs for selected samples in the validation set. The nine subfigures represent several important features that are present in the HYCOM results with and without tidal forcing and represent how the model performs in different oceanographic conditions. As mentioned previously, the tidal and nontidal HYCOM simulations cannot be considered paired data because of their mesoscale differences.

One notable feature of the model output is that the general structure of the temperature and salinity profiles is retained in the GAN translation. For example, in Figure 11a, a location off New England near the Gulf Stream, the tidally forced observations show a fresher, cooler region extending to 150 m depth that dissipates after approximately 90 hours. This is likely a mesoscale intrusion and is not present in the nontidal results. Thus, it is poorly represented when comparing the Global HYCOM (Exp. 19.0) to the GAN generated tidal fields.

The GAN model captures the periodic structure consistent with tidally forced simulations. This result is reminiscent of the orthogonal components demonstrated in Figure 10d-f. Interestingly, the amount of variability in the HYCOM simulations changes depending on the sample location. The DL model handles these differences consistently. For instance, Figure 11a has relatively strong periodic signatures in temperature and salinity and Figure 11b, located just to the south, has a weaker periodic structure. In both of these cases, the periodicity of the outputs of $G_{NT\rightarrow T}(\cdot)$ seem to match nicely with those from HYCOM Exp. 19.0 (tides). In contrast, in a location in the mid-North Atlantic further from the shelf (Figure 11i), there is weak periodic structure in tidal and non-tidal HYCOM, but the DL model artificially increases the periodic structure (most visible in water velocity). This location, located in the Gulf Stream extension away from shallow topography, likely has a small tidal signal and the periodic structure is more consistent with mesoscale eddy variability. This is an instance where the DL model imposes periodicity to make the sample like other tidally forced results, even though the actual HYCOM sample does not contain this structure.

As the data we are utilizing is unpaired, it is difficult to evaluate the performance of the model unless one visually inspects the outputs. In future work, a discriminator could be developed that could be trained to differentiate between these results. Since the model output used to train the DL models are sampled from a region of the globe during the same time of year, no two samples can be completely independent. This introduces the risk of overfitting. In further exploration of this topic, special care must be taken to ensure that data leakage is not occurring. Using unpaired data makes the model more robust to overfitting since the output has not been used in training but does not remove the risk entirely. Additionally, examination of the acoustic structure shows that there is a persistent offset in the sound-speed profiles between the GAN generated results and the original HYCOM (Exp. 19.0 and 19.2) simulations. Thus, although this work provides a good starting point, further work can be done to improve this DL approach.

5. Conclusions

The TFO-HYCOM project was a cross-disciplinary investigation into the modeling of internal tides and high-frequency IGWs, their sensitivity to model horizontal and vertical grid spacing, the energy transfer and dissipation of IGWs, the impacts of these structures on acoustics and the ability to model IGWs using DL techniques. During this project we examined the sensitivity of modeled IGWs to bathymetry and damping schemes and compared them to observations. The inclusion of internal tides in the models increases the high frequency SSH variability, and high-resolution bathymetry in models generates a stronger internal tide signal compared to low resolution models. We also examined the vertical mode decomposition, which demonstrated kinetic energy fluxes to higher harmonic internal waves and supertidal nonlinear internal waves. Internal wave dissipation was studied using spectral energy fluxes, which were in good agreement with observations. Spectral flux analysis of internal wave energy demonstrated the importance of internal wave and eddy interactions, which can also impact acoustics. Simulations run with and without tides showed clear differences in mean sound-speed structure and sound-speed variance, which was evident both in mesoscale features and at tidal frequencies. Simulations that included tidal forcing had greater sound-speed variance and were more consistent with observations. Tidal forcing directly impacted both acoustic parameters and acoustic propagation which were also sensitive to model vertical and horizontal resolution. To reduce computational cost, DL was used to parameterize tidal forcing and could reasonably introduce the periodicity of internal tides at a given location.

The inclusion of tidal forcing in ocean models improves the representation of the ocean state and its dynamics to better resemble observations. This has a direct impact on acoustic propagation by changing the sound speed at scales from 2 km to 100s of km, and time scales of hours to months. As global operational models begin to include tidal forcing it is important to understand how the model's horizontal and vertical grid spacing impact their representation of these physical processes, and how energy cascades through the internal wave spectrum. As running these models at high resolution are computationally expensive, parameterizing them using DL and other machine learning techniques may provide ways to better predict the impact of these processes on acoustic propagation using a coarser grid spacing or simulations without tidal forcing.

Acknowledgements:

This TFO-HYCOM project was funded by related Office of Naval Research (ONR) grants sent to the different institutions involved – N00014-19-1-2712 to University of Michigan, N00014-19-1-2717 to Florida State University, N00014-19-1-2704 to University of Southern Mississippi, N00014-20-C-2018 to ARiA and Applied Ocean Sciences, LLC, and contract number N00014-22WX00941 to the Naval Research Laboratory. We gratefully acknowledge ONR for their support of our research.

Author information:

Martha C. Schönau is a Senior Scientist at Applied Ocean Sciences, LLC.

Luna Hiron is a postdoc at the Center for Ocean-Atmospheric Prediction Studies at Florida State University.

John Ragland is a PhD student in the Department of Electrical and Computer Engineering at the University of Washington.

Keshav J. Raja is an Assistant Research Scientist at the Center for Ocean-Atmospheric Prediction Studies at Florida State University.

Joseph Skitka is a postdoc at the Department of Earth and Environmental Sciences at the

University of Michigan.

Miguel S. Solano is a postdoc at the School of Ocean Science and Engineering at the University of Southern Mississippi.

Xiaobiao Xu is a Senior Research Scientist at the Center for Ocean-Atmospheric Prediction Studies at Florida State University.

Brian K. Arbic is a professor in the Department of Earth and Environmental Sciences at the University of Michigan.

Maarten C. Buijsman is an associate professor at the School of Ocean Science and Engineering at the University of Southern Mississippi.

Eric P. Chassignet is a professor and director of the Center for Ocean-Atmospheric Prediction Studies at Florida State University

Emanuel Coelho is Chief Scientist at Applied Ocean Sciences, LLC.

Robert W. Helber is an oceanographer for the Naval Research Laboratory at the Stennis Space Center in Mississippi.

Jay F. Shriver is an oceanographer for the Naval Research Laboratory at the Stennis Space Center in Mississippi.

Jason Summers is the Chief Scientist at Applied Research in Acoustics, LLC (ARiA).

Kathryn L. Verlinden is a Senior Scientist at Applied Ocean Sciences, LLC (AOS).

Alan J. Wallcraft is a Research Scientist at the Center for Ocean-Atmospheric Prediction Studies at Florida State University.

Author Contributions

This manuscript highlights the research efforts by postdocs and early career researchers on the TFO-HYCOM project. Martha Schönau was the lead writer of this manuscript, project lead at her institution, and performed the research contributing to Figures 8 and 9a,b. Maarten Buijsman (Figure 2) Luna Hiron (Figure 3 and Figure 9c), John Ragland (Figures 10 and 11), Keshav J. Raja (part of Section 2), Joseph Skitka (Figure 6), Miguel S. Solano (Figures 1 and 4), Xiaobiao Xu (Figure 5), Jay Shriver and Bob Helber (Figure 6) performed research described in this document, and have submitted or will submit separate lead author papers that describe their research in more detail. Brian K. Arbic, Maarten C. Buijsman, Eric P. Chassignet, Emanuel Coelho, Robert W. Helber, Jay F. Shriver, and Jason E. Summers served as co-PIs of this TFO-HYCOM project at their respective institutions and oversaw the research efforts. Arbic conceived the idea of a project on internal wave impacts on acoustics, co-led the proposal writing, and organized regular online group meetings. Summers co-led the proposal writing for the project and served as lead principal investigator. Kathryn L. Verlinden provided ocean-atmospheric analysis in the Amazon region. Alan J. Wallcraft helped guide and run the Florida State University basin-wide Atlantic HYCOM simulations.

Figures:

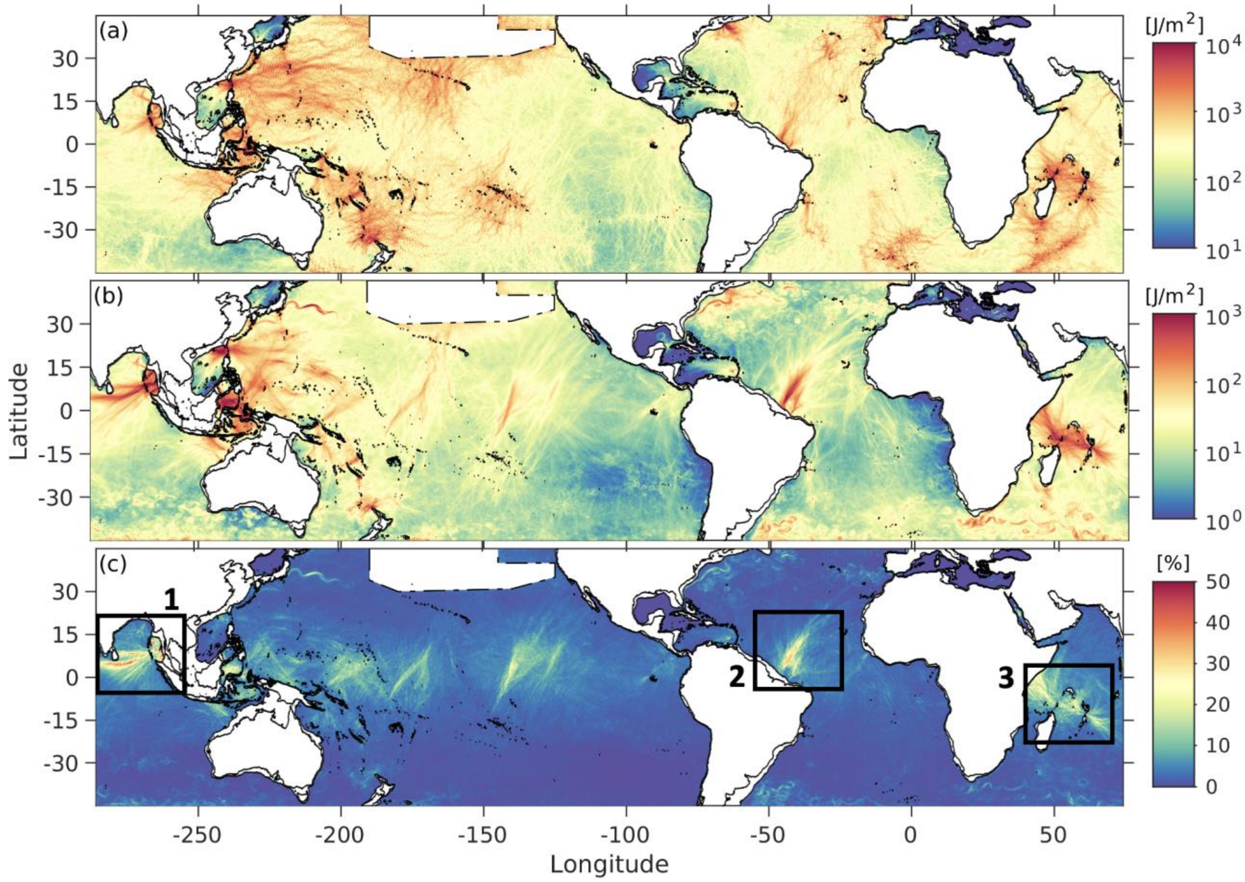

Figure 1: Time-mean and depth-integrated internal wave kinetic energy (J m^{-2}) band-passed at (a) semidiurnal and (b) supertidal frequency bands, as well as (c) the ratio of supertidal (KE_{HH}) to total (KE_{TOT}) energy as a percentage. Regions with relatively high supertidal energy (>20%) are indicated by the black rectangles: (1) the Bay of Bengal, (2) Amazon Shelf and (3) Mascarene Ridge.

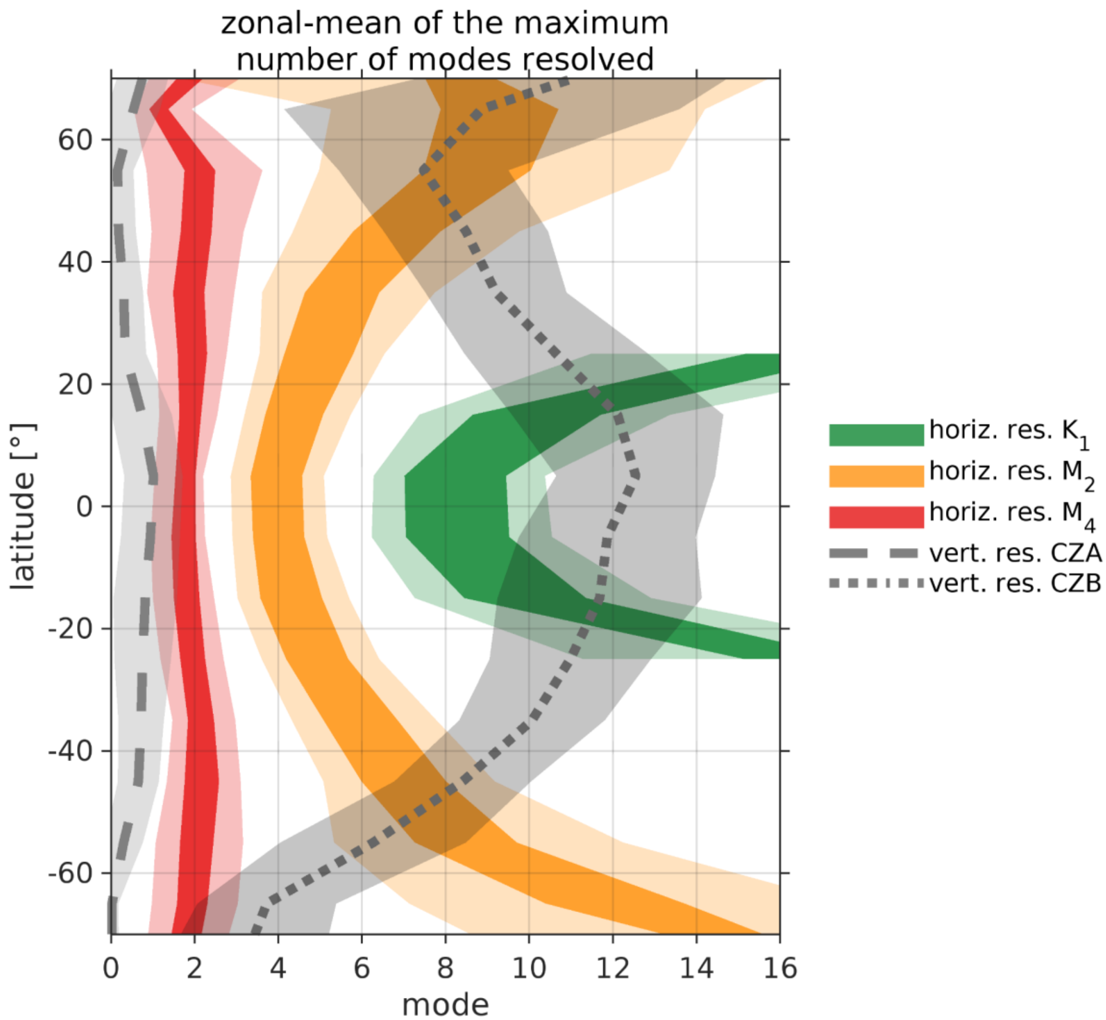

Figure 2. The predicted number of modes resolved for the horizontal resolution for various internal tide frequencies (colored polygons) and the vertical resolution (gray shaded polygons) area-averaged over longitude and 10° latitude bins. K_1, M_2, M_4 represent the dominant diurnal, semidiurnal, and supertidal constituents of internal tides with decreasing wavelengths, respectively. For the horizontal resolution, the dark-colored polygons mark the range of the number of resolved modes bounded by 6 and 8 cells/wavelength and the light-colored polygons mark the extent of the zonal-mean ± 1 standard deviation. For the vertical resolution, the dashed lines mark the zonal-means and the gray-shaded polygons mark the extent of the zonal-mean ± 1 standard deviation.

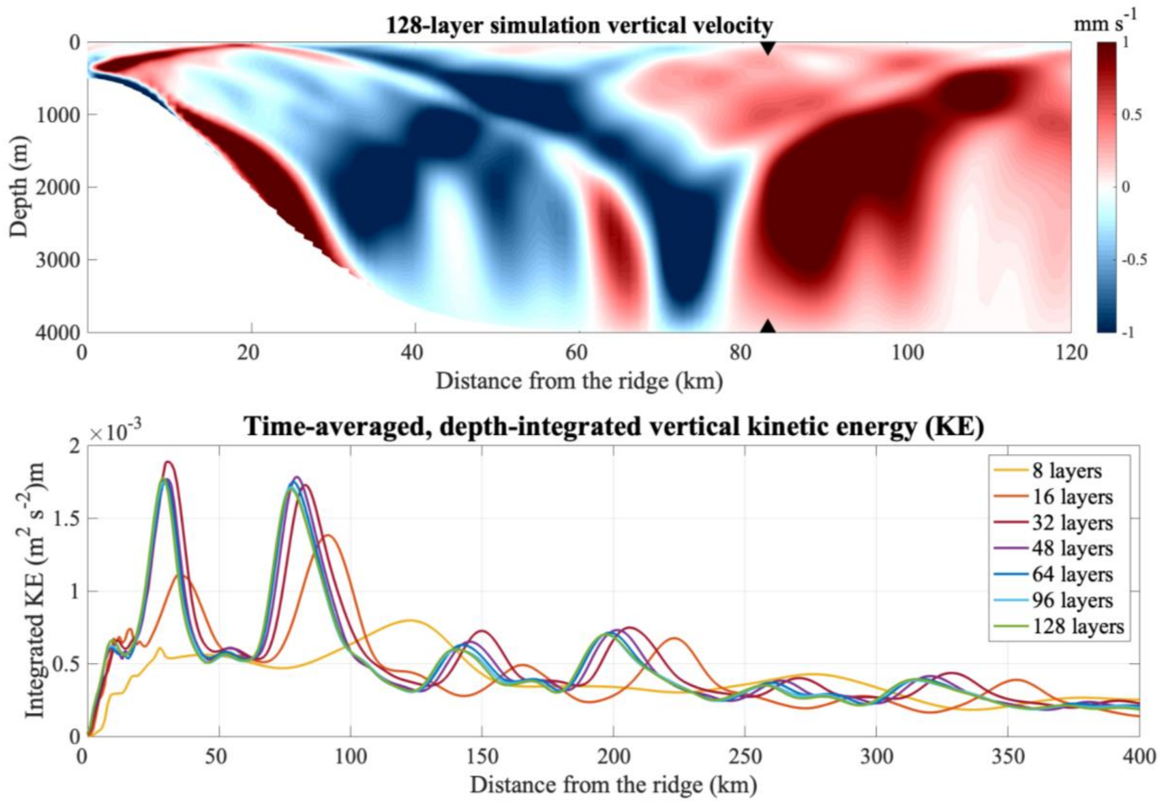

Figure 3. (Upper) Snapshot of the vertical velocity for the 128-layer simulation, zooming in closer to the ridge. The black triangles indicate the location where the sound speed profiles, shown in Fig. 9c, were computed. (Lower) Time-averaged, depth-integrated vertical kinetic energy ($\frac{1}{2}\int w^2 dz$) for different vertical discretizations: 8-, 16-, 32-, 48-, 64-, 96-, and 128-layers.

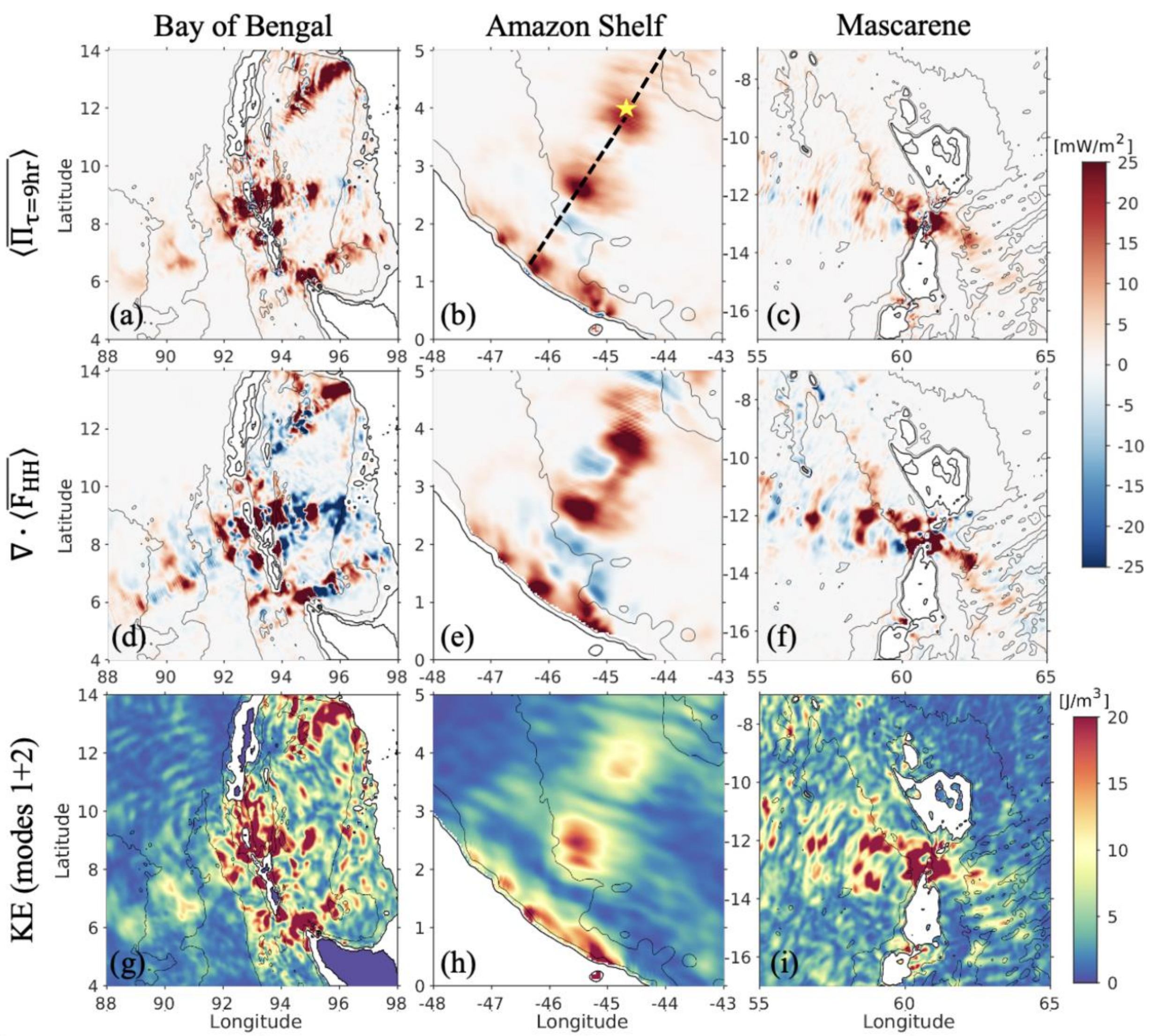

Figure 4: Time-mean and depth-integrated coarse-grained kinetic energy transfer ($\langle \Pi_{(\tau=9hr)} \rangle$) at (a) the Bay of Bengal and Andaman Sea, (b) Amazon Shelf and (c) Mascarene Ridge. Time-mean, depth-integrated divergence of supertidal energy flux ($\nabla \cdot \langle F_{HH} \rangle$) (d) the Bay of Bengal and Andaman Sea, (e) Amazon Shelf and (f) Mascarene Ridge. Time-mean surface kinetic energy for the superposition of modes 1+2 at the surface at (g) the Bay of Bengal and Andaman Sea, (h) Amazon Shelf and (i) Mascarene Ridge. Taken from Solano et al. (2023, submitted).

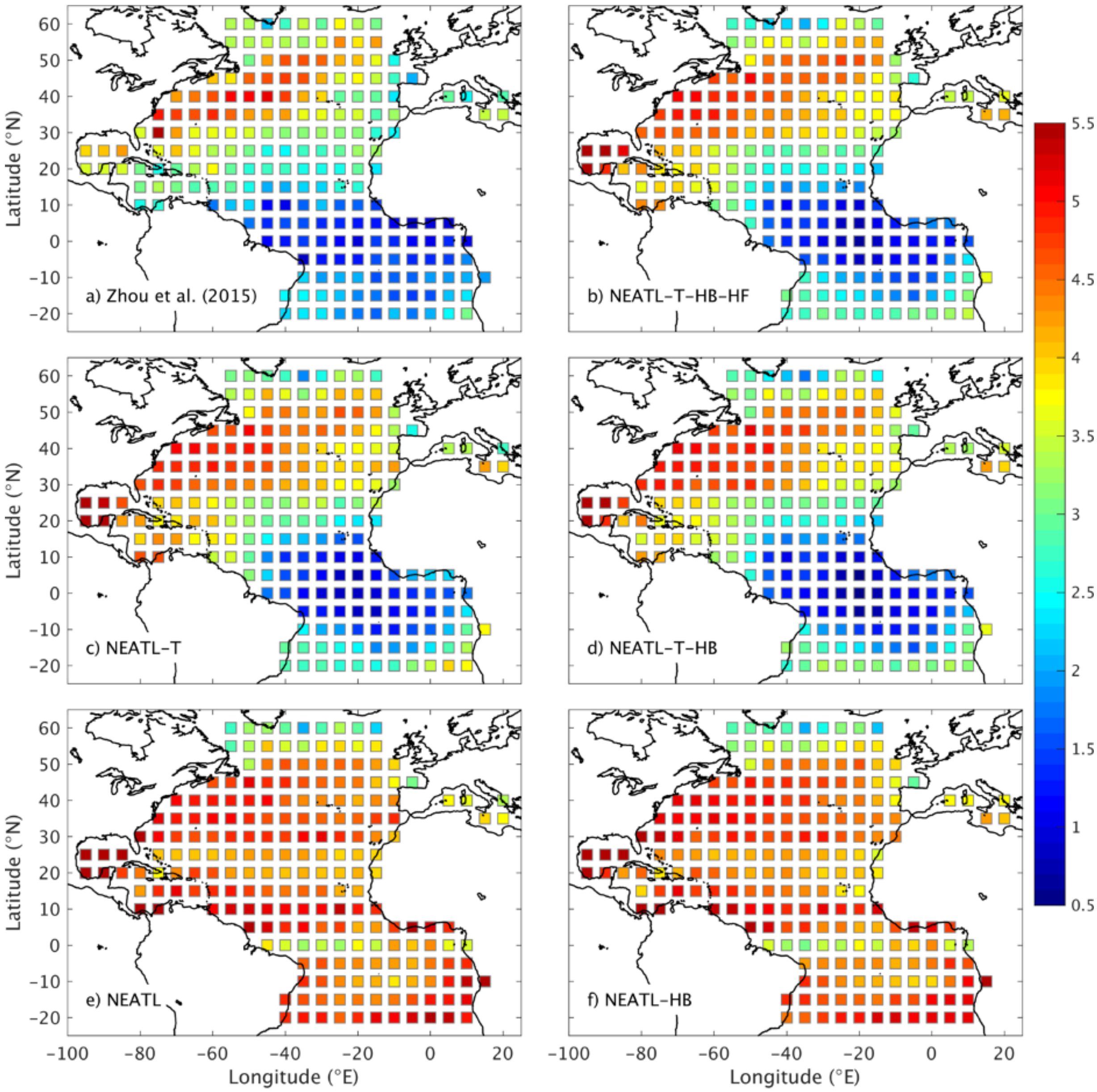

Figure 5. Mesoscale sea surface height (SSH) wavenumber spectral slope in the Atlantic Ocean based on a) satellite observations and b-f) a series of 1/50° numerical simulations (see Xu et al., 2022 for more detail). NEATL-T-HB-HF (with tides, high-resolution bathymetry, and high-frequency atmospheric forcing); NEATL-T (with tides); NEATL-T-HB (with tides, high-resolution bathymetry); NEATL (no tides); NEATL-HB (no tides, with high-resolution bathymetry). The result highlights that the large-scale spatial variability of the spectral slope is primarily due to the internal tides, whereas the impact of high-resolution bathymetry (difference between c & d) and high-frequency atmospheric forcing (difference between b & d) is relatively small. Taken from Xu et al. 2022, Figure 7. **Permission requested.**

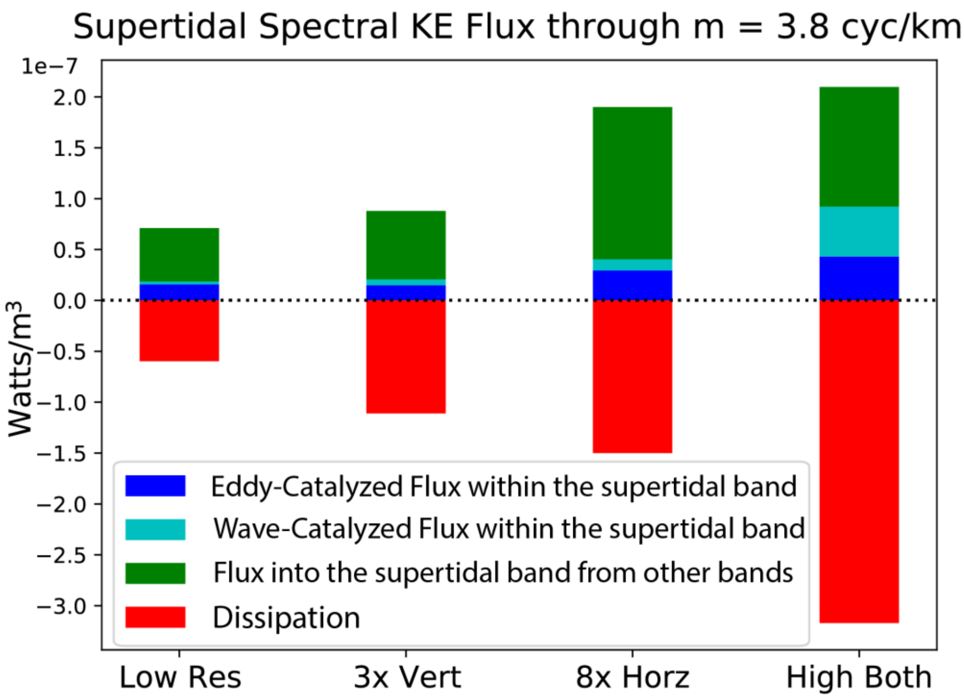

Figure 6: Vertical supertidal spectral kinetic-energy flux and integrated dissipation through a vertical wavenumber m = 3.8 cycles/km from a week of model output of a regional MITgcm ocean simulation in the North Pacific at different resolutions. Here, ω is the frequency of spectral modes in the flow and f_0 is the Coriolis frequency. A positive value of vertical supertidal spectral flux indicates downscale energy transport (based on the vertical length scale). The blue and cyan bars are the only two representing spectral flux within the supertidal continuum. The dissipation corresponds to an integrated spectral budget contribution of all sources of dissipation above m = 3.8 cycles/km and acts to remove energy flowing to small scales and should be in approximate balance to the positive fluxes. The "low-resolution" case has a horizontal grid spacing of 2 km and 88 vertical levels and other resolutions are given as relative to this base resolution. Adapted from Skitka et al. (2023, in review).

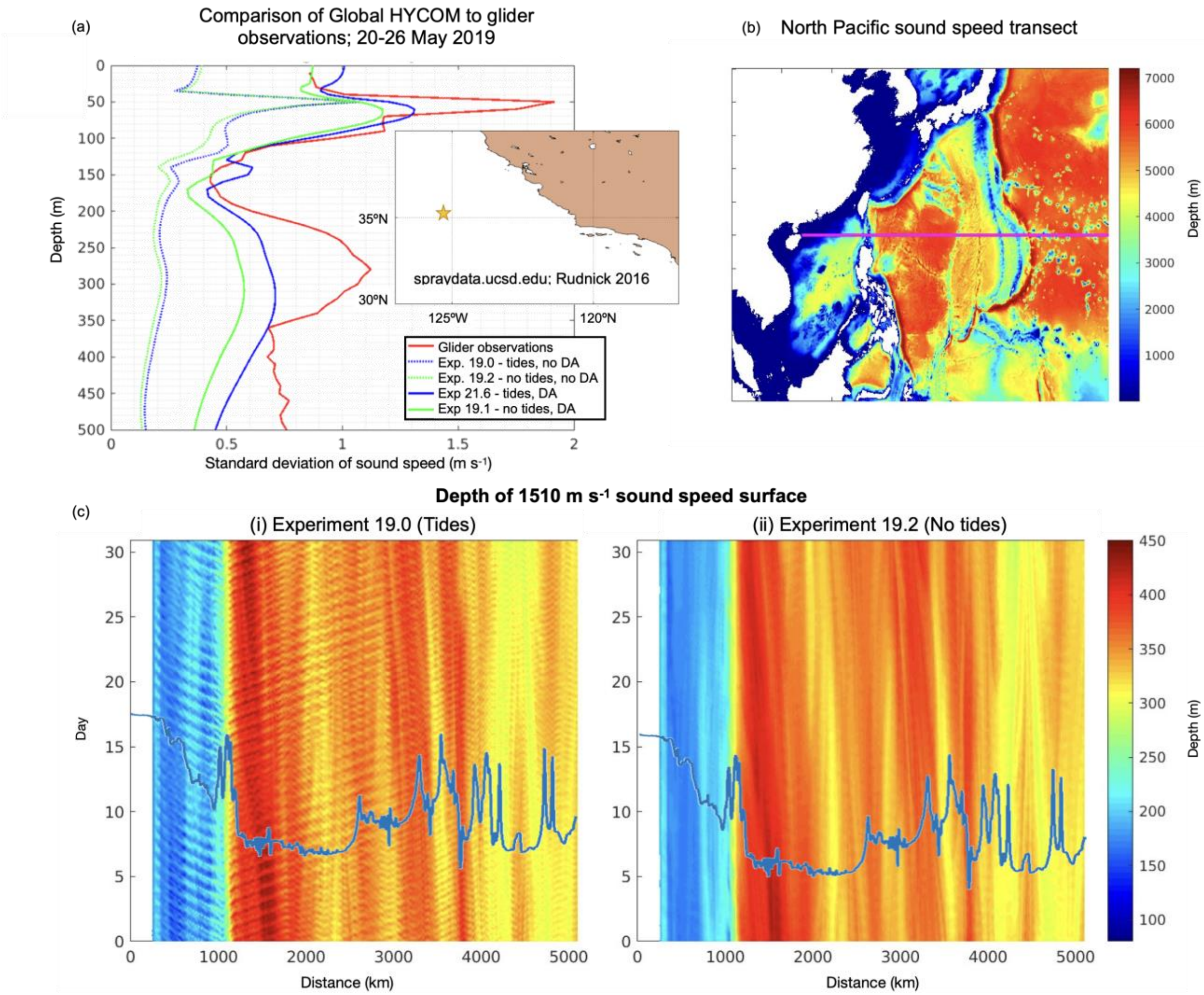

Figure 7: (a) Standard deviation of sound speed for 20-26 May 2019 from Global HYCOM simulations with and without tides and with and without data assimilation at location indicated on map of the coast of California. Simulations are compared to standard deviation computed from glider observations over the same week and location. (b) Map of transect (pink line) from the South China sea to the North Pacific, bisecting the Luzon Strait. (c) Bathymetry (blue line) overlaid on the depth of the 1510 m s-1 sound speed surface along the transect shown in (b) for each (i) Exp. 19.0 (tides) and (ii) Exp 19.2 (no tides). The Luzon Strait is located at 1000 km distance.

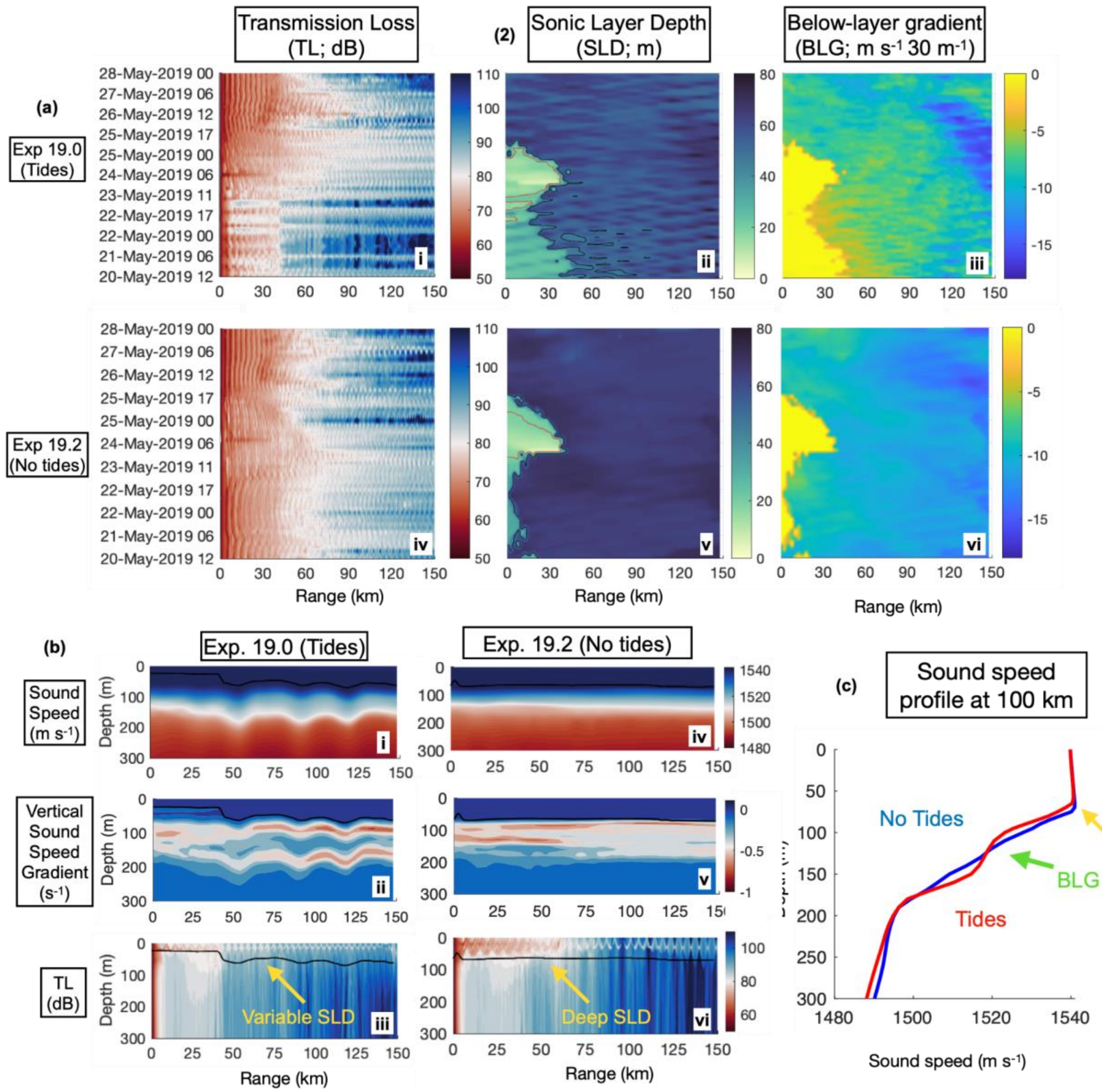

Figure 8: Comparison of acoustic propagation and properties between non-assimilative global HYCOM Exp.19.0 with tidal forcing and Exp.19.2 without tidal forcing. (a) Acoustic transmission loss (TL) at 20 m depth, sonic layer depth (SLD) and below-layer gradient (BLG) along a radial in the 60º direction (counterclockwise from east) from a 1500 Hz source at 20 m depth located in at 4.1ºN and 44.8ºW in the Amazon region for (i-iii) Exp. 19.0 (tides) and (iv-vi) Exp 19.2 (no tides). The location of the source and radial are along the line in Figure 4b (b) A snapshot from 20 May 2019 18:00:00 of (i, iv) sound speed (m s^{-1}) (ii, v) vertical gradient of sound speed (s^{-1}) and (iii,vi) TL (dB) from the source in (a) for (i-iii) Exp.19.0 and (iv-vi) Exp.19.2. (c) A single velocity profile at 100 km distance from the source along the 60º radial.

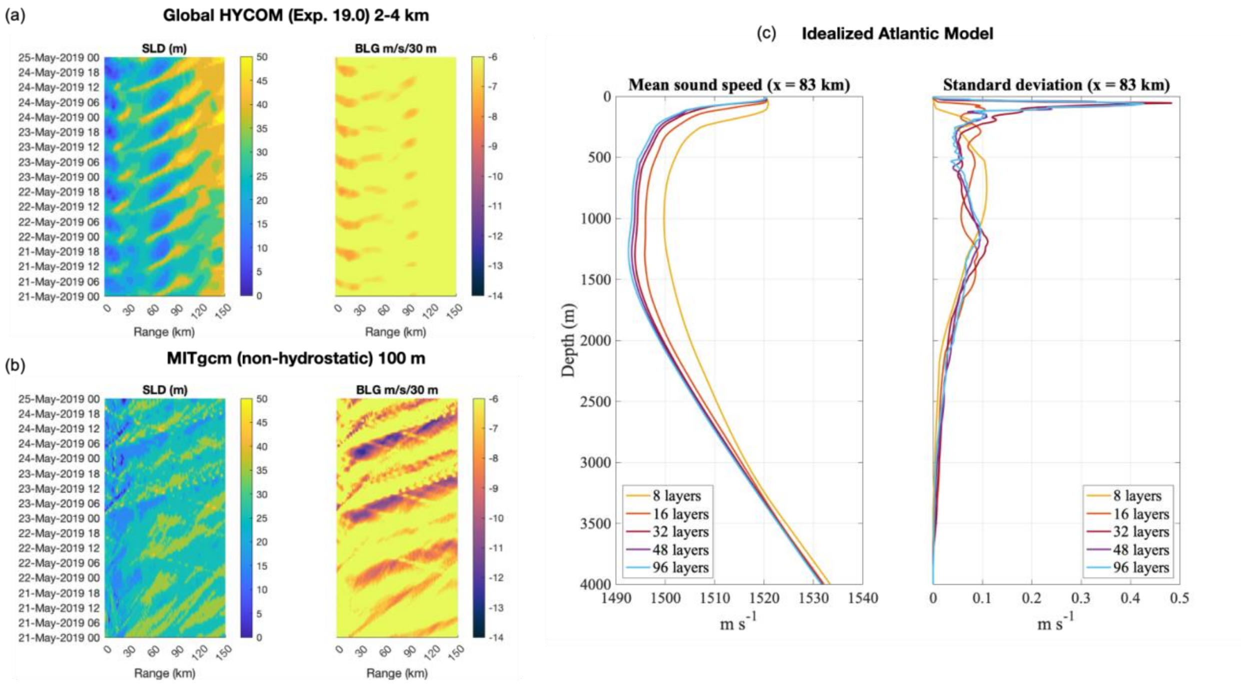

Figure 9: SLD and BLG for (a) global HYCOM Exp 19.0 and (b) a nonhydrostatic regional MITgcm simulation near the Mascarene Ridge (see Figure 4c). (c) Mean and standard deviation of sound speed from the idealized HYCOM model described in Section 2.2 at various vertical discretization (See Fig. 3a for the location of the profile).

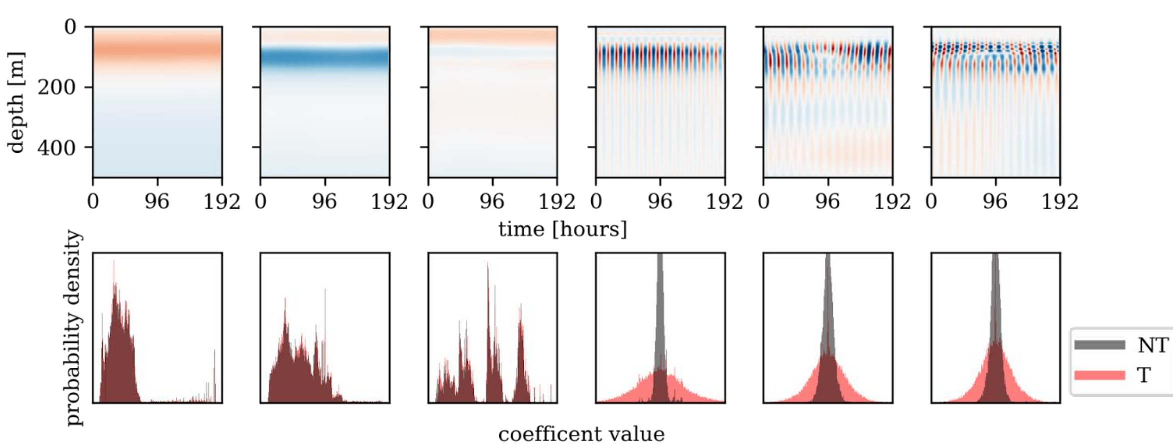

Figure 10. Plot of six selected orthogonal components of the non-tidal (NT) and tidal (T) model simulations and the associated distributions of coefficients for the NT and T data. Each column represents a single orthogonal component of water temperature as a function of depth and time. The top plot is the orthogonal component and the bottom plot is the distribution of coefficients for the NT and T data.

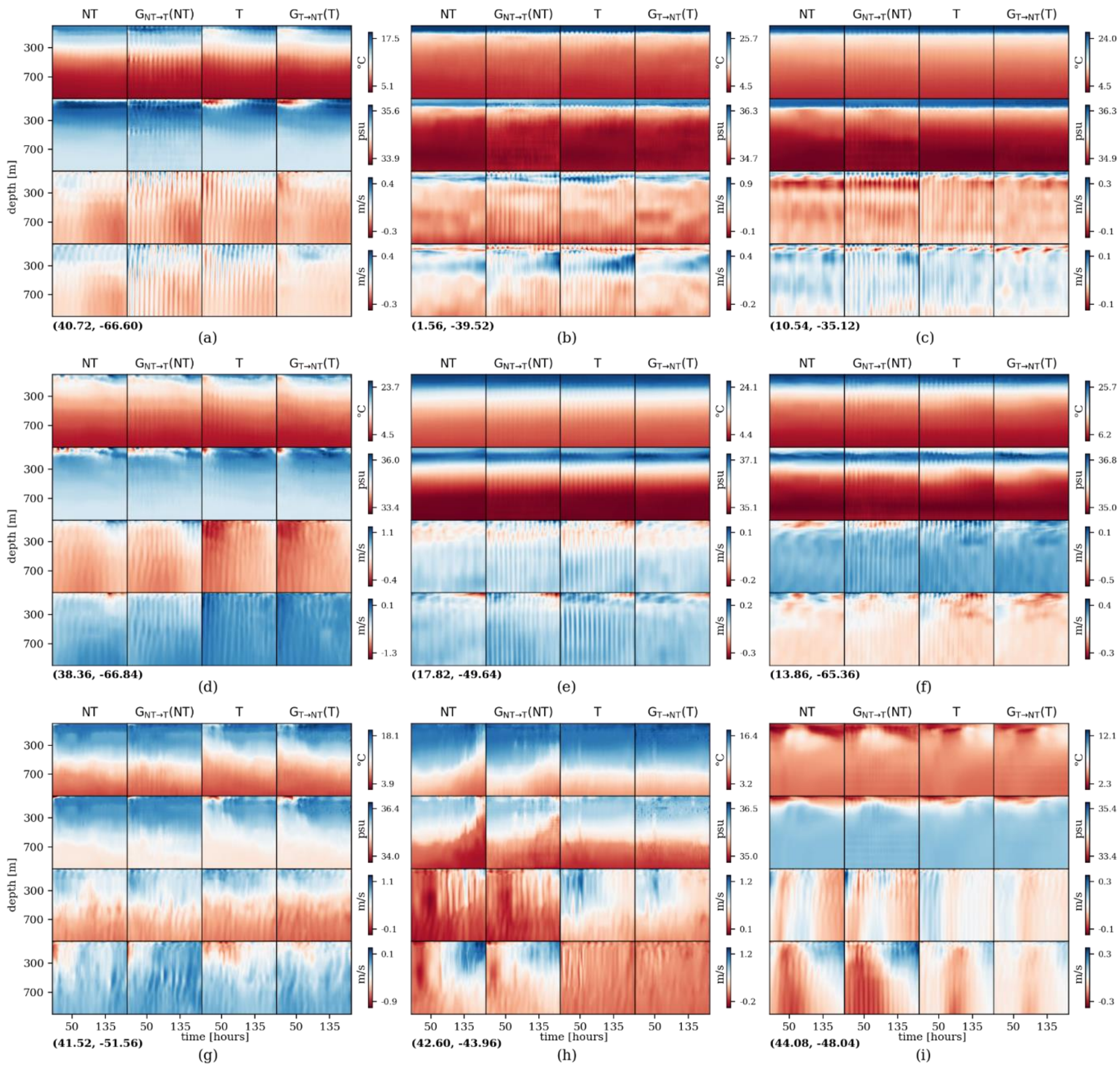

Figure 11. Temporal outputs of the trained DL model at the location noted in the bottom left of each subfigure (a)-(i). For each panel: the first column is the non-tidal (NT) HYCOM results (Exp 19.2); the second column is the NT results translated into the tidal domain using the DL model; the third column is the tidal (T) HYCOM results (Exp 19.0); the fourth column is the T results translated into the NT domain using the DL model. Each row corresponds to the oceanographic variables from top to bottom: water temperature, salinity, eastward velocity, and northward velocity respectively.

References:

Alford M.H., T. Peacock, J.A. MacKinnon, J.D. Nash, M.C. Buijsman, L.R. Centurioni, S.Y. Chao, M.H. Chang, D.M. Farmer, O.B. Fringer and others. 2015. The formation and fate of internal waves in the South China Sea. *Nature* 521(7550):65-9, doi: 10.1038/nature14399.

Ansong, J. K., B.K. Arbic, H.L. Simmons, M. H. Alford, M.C. Buijsman, P.G. Timko, A.J. Wallcraft. 2018. Geographical distribution of diurnal and semidiurnal parametric subharmonic instability in a global ocean circulation model. *Journal of Physical Oceanography* 48:1409-1431, https://doi.org/10.1016/j.pocean.2022.102824.

Arbic, B.K., S.T. Garner, R.W. Hallberg, H.L. Simmons. 2004. The accuracy of surface elevations in forward global barotropic and baroclinic tide models. *Deep-Sea Research II* 51:3069–3101, https://doi.org/10.1016/j.dsr2.2004.09.014.

Arbic, B.K, J.G. Richman, J.F. Shriver, P.G. Timko, E.J. Metzger, and A.J. Wallcraft. 2012. Global modeling of internal tides within an eddying ocean general circulation model. *Oceanography*, 25, 20-29, https://doi.org/10.5670/oceanog.2012.38.

Arbic, B.K., M.H. Alford, J.K. Ansong, M.C. Buijsman, R.B. Ciotti, J.T. Farrar, R.W. Hallberg, C.E. Henze, C.N. Hill, C.A. Luecke and others. 2018. A primer on global internal tide and internal gravity wave continuum modeling in HYCOM and MITgcm. In *New frontiers in operational oceanography*, E. Chassignet, A. Pascual, J. Tintore, and J. Verron, Eds., GODAE OceanView, 307-392, https://doi.org/10.17125/gov2018.ch13**.**

Arbic, B.K. 2022. Incorporating tides and internal gravity waves within global ocean general circulation models: A review. *Progress in Oceanography* 206:102824, https://doi.org/10.1016/j.pocean.2022.102824.

Arbic, B.K., S. Elipot, J.M. Brasch, D. Menemenlis, A.L. Ponte, J.F. Shriver, X. Yu, E.D. Zaron, M.H. Alford, M.C. Buijsman and others. 2022. Near-surface oceanic kinetic energy distributions from drifter observations and numerical models. *Journal of Geophysical Research: Oceans* 127: e2022JC018551, https://doi.org/10.1029/2022JC01855.

Bleck, R., 2002. An oceanic general circulation model framed in hybrid isopycnic Cartesian coordinates. *Ocean Modelling* 4:5588. https://doi.org/10.1016/S1463-5003(01)00012-9.

Buijsman, M. C., Y. Kanarska, and J.C. McWilliams. 2010. On the generation and evolution of nonlinear internal waves in the South China Sea, *Journal of Geophysical Research* 115:C02012, doi:10.1029/2009JC005275.

Buijsman, M., G.R. Stephenson, J.K. Ansong, B.K. Arbic, M. Green, J.G. Richman, J.F. Shriver, and others. 2020. On the interplay between horizontal resolution and wave drag and their effect on tidal baroclinic mode waves in realistic global ocean simulations. *Ocean Modelling* 152:101656, https://doi.org/10.1016/j.ocemod.2020.101656.

Buijsman, M., M. Solano, J.F. Shriver, *In Preparation.* Variance in baroclinic modes across frequency bands in a global ocean simulation. Ocean Modelling.

Chassignet, E. P., L. T. Smith, G. R. Halliwell, and R. Bleck. 2003. North Atlantic Simulations with the Hybrid Coordinate Ocean Model (HYCOM): Impact of the Vertical Coordinate Choice, Reference Pressure, and Thermobaricity. *Journal of physical oceanography* 33:2504–2526, https://doi.org/10.1175/1520-0485(2003)033<2504:NASWTH>2.0.CO;2.

Chassignet, E.P., H.E. Hurlburt, E.J. Metzger, O.M. Smedstad, J.A. Cummings, G.R. Halliwell, R. Bleck, R. Baraille, A.J. Wallcraft, C. Lozano, H.L. Tolman, A. Srinivasan, S. Hankin, P. Cornillon, R. Weisberg, A. Barth, R. He, F. Werner, and J. Wilkin. 2009. US GODAE: Global ocean prediction with the HYbrid Coordinate Ocean Model (HYCOM). *Oceanography* 22(2):64–75, https://doi.org/10.5670/oceanog.2009.39.

Chassignet, E. P., and Xu, X. 2017. Impact of horizontal resolution (1/12° to 1/50°) on Gulf Stream separation, penetration, and variability. *Journal of Physical Oceanography* 47:1999−2021, https://doi.org/10.1175/JPO-D-17-0031.1.

Creswell, A., T. White, V. Dumoulin, K. Arulkumaran, B. Sengupta and A. A. Bharath. 2018. Generative Adversarial Networks: An Overview. *IEEE Signal Processing Magazine*, 35(1):53-65, doi: 10.1109/MSP.2017.2765202.

Cummings, J.A. and O.M Smedstad. 2013. Variational data assimilation for the global ocean. Pp.303-343 in *Data Assimilation for Atmospheric, Oceanic and Hydrologic Applications* (*Vol. II)* doi: 10.1007/978-3-642-35088-7_13, Springer-Verlag Berlin Heidelberg.

Dufau, C., M. Orsztynowicz, G. Dibarboure, R. Morrow, P.-Y. Le Traon. 2016. Mesoscale resolution capability of altimetry: Present and future. Journal of Geophysical Research. *Oceans* 121:4910–4927, https://doi.org/10.1002/2015JC010904.

Dematteis, G., K. Polzin, and Y. V. Lvov. 2022. On the origins of the oceanic ultraviolet catastrophe. *Journal of Physical Oceanography* 52(4):597–616, https://doi.org/10.1175/JPO-D-21-0121.1.

Eden, C., F. Pollmann, and D. Olbers. 2020. Towards a Global Spectral Energy Budget for Internal Gravity Waves in the Ocean, *Journal of Physical Oceanography* 50(4):935-944, https://doi.org/10.1175/JPO-D-19-0022.1

Egbert, G.D., A.F. Bennett and M.G.G Foreman. 1994. Topex/Poseidon tides estimated using a global inverse model. *Journal of Geophysical Research* 99:24821–24852, https://doi.org/10.1029/94JC01894.

Garrett, C., and E. Kunze, 2007. Internal Tide Generation in the Deep Ocean. *Annual Review of Fluid Mechanics* 39(1):57-87. Doi: 10.1146/annurev.fluid.39.050905.110227.

Garrett, C., and W. Munk. 1979. Internal waves in the ocean. *Annual Review of Fluid Mechanics*, 11(1):339–369, https://doi.org/10.1146/annurev.fl.11.010179.002011.

Geoffroy, G., J. Nycander, M.C. Buijsman, J.F. Shriver, and B.K. Arbic. 2022. Validating the spatial variability of the semidiurnal internal tide in a realistic global ocean simulation with Argo and mooring data. *EGUsphere [preprint]*, https://doi.org/10.5194/egusphere-2022-1085.

Gill, Adrian E. 1982. *Atmosphere-ocean dynamics.* Vol. 30. Academic press, London, UK, 1982.

Goodfellow, I. J., J. Pouget-Abadie, M. Mirza, B. Xu, D. Warde-Farley, S. Ozair, A. Courville, and Y Bengio. 2014. Generative Adversarial Networks. *ArXiv:1406.2661 [Cs, Stat]*. http://arxiv.org/abs/1406.2661

Goodfellow, I., Bengio, Y., & Courville, A. (2016). *Deep Learning*. MIT Press. http://www.deeplearningbook.org

Helber, R. W., C.N. Barron, M.R. Carnes and R.A. Zingarelli. 2008. Evaluating the sonic layer depth relative to the mixed layer depth. *Journal of Geophysical Research* 113:C07033. doi:10.1029/2007JC004595.

Hogan, T.F., M. Liu, J.A. Ridout, M.S. Peng, T.R. Whitcomb, B.C. Ruston, C.A. Reynolds, S.D. Eckermann, J.R. Moskaitis, N.L. Baker, J.P. McCormack, K.C. Viner, J.G. McLay, M.K. Flatau, L. Xu, C. Chen, and S.W. Chang. 2014. The Navy Global Environmental Model. *Oceanography* 27(3):116–125, https://doi.org/10.5670/oceanog.2014.73.

Kelly, S. M., A. F. Waterhouse, and A. C. Savage. 2021. Global dynamics of the stationary M2 Mode-1 internal tide. *Geophysical Research Letters* 48:e2020GL091692, doi: 10.1029/2020GL091692.

Lamb, K. G. 2004. Nonlinear interaction among internal wave beams generated by tidal flow over supercritical topography, *Geophysical Research Letters* 31:L09313, doi:10.1029/2003GL019393.

Luecke, C.A., B.K. Arbic, J.G. Richman, J.F. Shriver, M.H. Alford, J.K. Ansong, S.L. Bassette, M.C. Buijsman, D. Menemenlis, R.B. Scott, and others. 2020. Statistical comparisons of temperature variance and kinetic energy in global ocean models and observations: Results from mesoscale to internal wave frequencies. *Journal of Geophysical Research: Oceans* 125:e2019JC015306, https://doi.org/10.1029/2019JC015306.

Marshall, J., A. Adcroft, C. Hill, L. Perelman, C. Heisey. 1997. A finite-volume, incompressible Navier Stokes model for studies of the ocean on parallel computers. *Journal of Geophysical Research* 102:5753–5766, https://doi.org/10.1029/96JC02775.

Mejjati, Y. A., C. Richardt, J. Tompkin, D. Cosker, and K.I. Kim. 2018. Unsupervised Attention-guided Image to Image Translation (arXiv:1806.02311). arXiv. https://doi.org/10.48550/arXiv.1806.02311

Metzger, E.J., O.M. Smedstad, P.G. Thoppil, H.E. Hurlburt, J.A. Cummings, A.J. Wallcraft, L. Zamudio, D.S. Franklin, P.G. Posey, M.W. Phelps, P.J. Hogan, F.L. Bub, and C.J. DeHaan. 2014. US Navy operational global ocean and Arctic ice prediction systems. *Oceanography* 27(3):32–43, http://dx.doi.org/10.5670/oceanog.2014.66.

McComas, C. H., and F. P. Bretherton. 1977. Resonant interaction of oceanic internal waves. *Journal of Geophysical Research* 82(9):1397–1412, https://doi.org/10.1029/JC082i009p01397.

Naval Meteorology and Oceanography Command (1986), Fleet Oceanographic and Acoustic Reference Manual.

Nelson, A., B. Arbic, D. Menemenlis, W. Peltier, M. Alford, N. Grisouard, and J. Klymak. 2020. Improved internal wave spectral continuum in a regional ocean model. *Journal of Geophysical Research: Oceans* 125(5), https://doi.org/10.1029/2019JC015974.

Ngodock, H. E., I. Souopgui, A. J. Wallcraft, J. G. Richman, J. F. Shriver, and B. K. Arbic. 2016. On improving the accuracy of the barotropic tides embedded in a high-resolution global ocean circulation model. *Ocean Modelling* 97:16-26, https://doi.org/10.1016/j.ocemod.2015.10.011

Pan, Y., B.K. Arbic, A.D. Nelson, D. Menemenlis, W.R. Peltier, W. Xu, and Y Li. 2020. Numerical investigation of mechanisms underlying oceanic internal gravity wave power-law spectra. *Journal of Physical Oceanography* 50:2713–2733. https://doi.org/10.1175/ JPO-D-20-0039.1.

Polzin, Kurt L., and Yuri V. Lvov. 2011. Toward regional characterizations of the oceanic internal wavefield." *Reviews of Geophysics* 49(4).

Porter, Michael. 2011. The BELLHOP Manual and User's Guide: PRELIMINARY DRAFT. http://oalib.hlsresearch.com/Rays/HLS-2010-1.pdf. Accessed 23 March 2023.

Raja, K. J., M.C. Buijsman, J.F. Shriver, B.K. Arbic and O. Siyanbola. 2022. Near-inertial wave energetics modulated by background flows in a global model simulation. *Journal of Physical Oceanography* 52(5):823-840.

Raja, K. J., M. Buijsman, A. Bozec, R.W. Helber, J.F. Shriver, A. Wallcraft, E.P. Chassignet, B.K. Arbic. 2023. Spurious internal wave generation during data assimilation in eddy resolving ocean model simulations. Ocean Modelling., submitted.

Rudnick, D. 2016. California Underwater Glider Network [Data set]. Scripps Institution of Oceanography, Instrument Development Group. doi: 10.21238/S8SPRAY1618

Siedler, G., S.M. Griffies, J. Gould, and J. A. Church (Eds.). 2013. *Ocean Circulation and Climate – A 21st Century Perspective*. Elsevier - Academic Press, Amsterdam.

Simmons, H.L., R.W. Hallberg, B.K. Arbic. 2004. Internal wave generation in a global baroclinic tide model. *Deep-Sea Research II*, 51:3043–3068. https://doi.org/10.1016/j. dsr2.2004.09.015.

Skitka, J., B.K. Arbic, R. Thakur, D. Menemenlis, W.R. Peltier, Y. Pan, K. Momeni, and Y Ma. 2022. Probing the nonlinear interactions of supertidal internal waves using a high-resolution regional ocean model. In Review.

Solano, M., M.C. Buijsman, J.F. Shrive, J. Magalhaes, J.C. Da Silva, C. Jackson, B.K. Arbic, R. Barkan. 2023. Nonlinear internal tides in a realistically forced global ocean simulation. *Journal of Geophysical Research*, submitted.

Stewart, K.D., A.M.C. Hogg, S.M. Griffies, A.P. Heerdegen, M.L. Ward, P. Spence, M.H. England. 2017. Vertical resolution of baroclinic modes in global ocean models. *Ocean Modelling* 113:50–65, doi:10.1016/j.ocemod.2017.03.012.

Thakur, R., B.K. Arbic, D. Menemenlis, K. Momeni, Y. Pan, W.R. Peltier, J. Skitka, M.H. Alford, and Y. Ma, 2022: Impact of vertical mixing parameterizations on internal gravity wave spectra in regional ocean models. *Geophysical Research Letters* 49:e2022GL099614, https://doi.org/10.1029/2022GL099614

Xu, X., E.P. Chassignet, A.J. Wallcraft, B.K. Arbic, M.C. Buijsman and M. Solano. 2022. On the spatial variability of the mesoscale sea surface height wavenumber spectra in the Atlantic Ocean. *Journal of Geophysical Research: Oceans* 127:e2022JC018769, https://doi.org/10.1029/2022JC018769

Xu, Y., and Fu, L.-L. 2012. The effects of altimeter instrument noise on the estimation of the wavenumber spectrum of sea surface height. *Journal of Physical Oceanography* 42:2229–2233, https://doi.org/10.1175/JPO-D-12-0106.1.

Zhou, X.-H., D.-P Wang, and D. Chen. 2015. Global wavenumber spectrum with corrections for altimeter high frequency noise. *Journal of Physical Oceanography* 45(2):495-503, https://doi.org/10.1175/JPO-D-14-0144.1.

Zhu, J. Y., T. Park, P. Isola, and A.A. Efros. 2017. Unpaired image-to-image translation using cycle-consistent adversarial networks. Pp. 2223-2232 in *Proceedings of the IEEE international conference on computer vision*. Venice, Italy. doi: 10.1109/ICCV.2017.244.